



Spherical aberration correction in a scanning transmission electron microscope using a sculpted thin film

Roy Shiloh^{a,1,*}, Roei Remez^{a,1}, Peng-Han Lu^{b,1}, Lei Jin^b, Yossi Lereah^a, Amir H. Tavabi^b, Rafal E. Dunin-Borkowski^b, Ady Arie^a

^a School of Electrical Engineering, Fleischman Faculty of Engineering, Tel Aviv University, Tel Aviv, Israel

^b Ernst Ruska-Centre for Microscopy and Spectroscopy with Electrons and Peter Grünberg Institute, Forschungszentrum Jülich, Jülich, Germany

ARTICLE INFO

Article history:

Received 23 December 2017

Revised 18 March 2018

Accepted 24 March 2018

Available online 27 March 2018

ABSTRACT

Nearly eighty years ago, Scherzer showed that rotationally symmetric, charge-free, static electron lenses are limited by an unavoidable, positive spherical aberration. Following a long struggle, a major breakthrough in the spatial resolution of electron microscopes was reached two decades ago by abandoning the first of these conditions, with the successful development of multipole aberration correctors. Here, we use a refractive silicon nitride thin film to tackle the second of Scherzer's constraints and demonstrate an alternative method for correcting spherical aberration in a scanning transmission electron microscope. We reveal features in Si and Cu samples that cannot be resolved in an uncorrected microscope. Our thin film corrector can be implemented as an immediate low cost upgrade to existing electron microscopes without re-engineering of the electron column or complicated operation protocols and can be extended to the correction of additional aberrations.

© 2018 The Authors. Published by Elsevier B.V.

This is an open access article under the CC BY-NC-ND license.

(<http://creativecommons.org/licenses/by-nc-nd/4.0/>)

1. Introduction

The development of the transmission electron microscope (TEM) [1] heralded a new age in the characterization of the atomic structure of matter. However, for many years its spatial resolution was limited to approximately 100 times the electron wavelength, in contrast to light optics, where sub-wavelength diffraction limited resolution is now readily available. The problem originates from the unavoidable, positive spherical aberration of electron lenses, as described by Otto Scherzer in his 1936 seminal paper [2]. His theorem is based on a number of constraints, including the fact that electromagnetic fields generated by round lenses are axially symmetric and static and that the neighborhood of the optical axis is charge-free. He subsequently made several proposals for correcting spherical aberration by relaxing these constraints [3]. However, it was only two decades ago that Haider et al. [4] and Krivanek et al. [5] finally succeeded in experimentally correcting spherical aberration in the imaging and probe-forming lenses of electron microscopes, respectively, by using non-rotationally-symmetric multipole correctors. For the first time, researchers could obtain directly

interpretable images of atomic columns in materials in both TEM and scanning TEM (STEM). The advent of high brightness electron guns and an improved ability to overcome noise and to resolve features in (S)TEM images was a catalyst for a multitude of new applications of electron microscopy [6]. However, multipole aberration correctors still require precise manufacture, accurate alignment, major changes to the electron column, stable power supplies, additional water cooling, and dedicated operation protocols. Thus, the only practical way to improve the resolution of an uncorrected microscope is to replace it altogether, at considerable cost, by a new aberration corrected microscope. Considerable effort had also previously been devoted to realizing spherical aberration correction using charged foils, electrodes, and meshes [7], which rely on the presence of a charge distribution to generate negative spherical aberration either at the gun [8] or at the objective lens [9]. Unfortunately, such solutions are difficult to realize, in part due to their short lifetime under intense electron bombardment and a high contamination rate. An alternative approach was proposed as early as 1947 by Boersch [10], who suggested to use the mean inner potential and thickness of a material to impart a phase shift to an electron beam. The mean inner potential is related to the charge density distribution in a material [11], and can therefore be used to violate Scherzer's charge-free constraint. Although extensive research was carried out in this direction [12], attempts to

* Corresponding author.

E-mail address: royshilo@post.tau.ac.il (R. Shiloh).

¹ These authors contributed equally to this work.

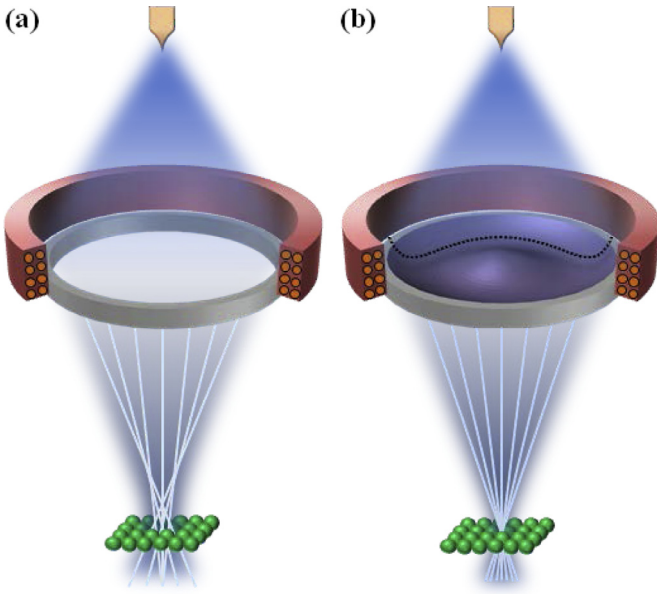


Fig. 1. Schematic diagrams showing the setup for aberration correction using a thin film corrector. (a) An electron probe formed using a standard limiting aperture is affected significantly by spherical aberration. (b) Equal but opposite spherical aberration is introduced by a thin film corrector, yielding a spherical-aberration-free probe. The corrector comprises a membrane of radially-varying thickness (dotted black line).

fabricate phase-shifting thin films that act as electron lenses [13–15] were never successfully translated into practice. Here, we describe how the primary spherical aberration of the probe-forming optics in a STEM can now be corrected by using a continuous, refractive design. To this end, we employ a silicon nitride thin film [16–18] that is machined with nanometer precision using focused ion beam (FIB) milling (see 3). Our thin film corrector can be fabricated at a tiny fraction of the complexity of an electromagnetic multipole corrector.

Fig. 1 shows a schematic diagram of our solution, which involves passing the electron beam through a nanofabricated refractive film of varying thickness. In an uncorrected microscope (Fig. 1a), the electron beam is affected by spherical aberration as it passes through the probe-forming electromagnetic lenses and limiting aperture (here, the Condenser 2 aperture in an FEI microscope). We replace this Pt aperture with a compact thin film corrector (Fig. 1b), which introduces spherical aberration of the opposite sign, in order to form a spherical-aberration-corrected probe at the sample plane.

Spherical aberration is the dominant aberration of electron-optical lenses. The phase due to spherical aberration and defocus can be written in the form

$$\chi = \frac{\pi}{2\lambda} C_s (\theta^4 - 2\Delta z \theta^2), \quad (1)$$

where θ is the beam's semi-angle with respect to the optical axis, Δz is the defocus, C_s is the spherical aberration coefficient and λ is the electron wavelength [3]. The value of Δz in Eq. (1) can be chosen arbitrarily. In order to minimize the change in the phase aberration χ at the edge of the aperture, it can be chosen to be equal to the Scherzer defocus $\Delta z = 0.5C_s\alpha^2$, where α is the convergence semi-angle. Furthermore, we can then define a 2π phase shift as *one cycle* (abbreviated “1 λ ”) and characterize the maximal phase difference introduced by χ using the figure of merit “*peak-to-valley*” wavefront error [19], calculated as $\Lambda = C_s\alpha^4/16\lambda$ cycles.

An electron beam passing through a non-magnetic thin film accumulates a phase shift that depends on its thickness t according

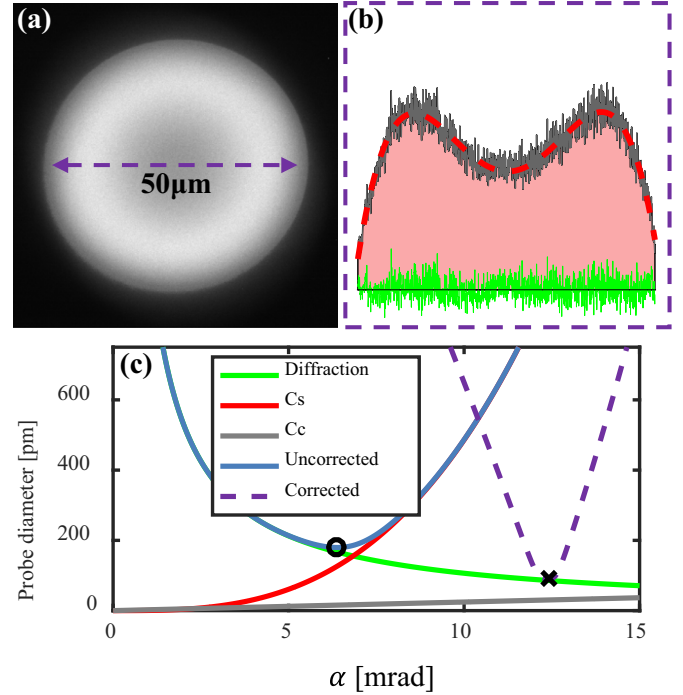


Fig. 2. (Colour online) Design and measurement of a thin film corrector. (a) Intensity TEM image of the installed corrector. Higher intensity corresponds to thinner material. (b) Intensity cross-section (black), fit to a fourth degree polynomial (dashed red) and residuals (green). (c) The *geometric* diameter of a probe plotted as a function of the probe-forming optics' convergence semi-angle α . The diffraction contribution (green) is inversely proportional to the diameter of the probe, spherical aberration (red) has a cubic dependence, while the contribution from chromatic aberration (gray) has a linear dependence. The combined effect is calculated as a root power sum (blue), resulting in an optimum “o” (6.4 mrad / 180 pm). When using the corrector (dashed purple), the optimal value is estimated at “x” (12.4 mrad / 91 pm).

to the expression

$$\varphi = C_E U_i t, \quad (2)$$

where U_i is the film's mean inner potential and C_E is a constant that depends on the electron energy. In order to negate spherical aberration, the thickness profile must satisfy the relation $\varphi = -\chi$. If $t_{2\pi}$ is defined to be the required thickness for a phase shift of one cycle, then the thickness profile of the thin film corrector is given by the expression

$$t(r) = t_{2\pi} \times \frac{4\Lambda}{r_{max}^4} (r^4 - r^2 r_{max}^2), \quad (3)$$

where r_{max} is the radius of the corrector's limiting aperture, or aperture stop, *i.e.*, the radius that defines the probe-forming optics' convergence semi-angle α . Our defocus choice in Eq. (1) also minimizes the design thickness. In practice, a small fraction of the film thickness supports the structure mechanically and remains uncorrected.

2. Corrector design

We previously investigated fractured (modulo- 2π) designs of phase masks [17]. Here, we fabricated continuous, non-fractured thin film elements (see Fig. 2a), restricting ourselves to a maximum thickness of $2t_{2\pi}$. This approach eliminates difficulties associated with sharp edges (see discussion in [17]), and removes the limitation of using a single accelerating voltage. From Eq. (3), for $t = 2t_{2\pi}$ the peak-to-valley value is $\Lambda = 2$, so up to 2λ of aberrations can be corrected. Although a thicker design allows stronger correction, it would also result in increased electron scattering and

therefore a corrected probe with lower current. A possible remedy would be to enlarge the corrector diameter or replace the material [20]. A thinner design would reduce scattering and increase contrast, but provide less correction. For the present parameters, solving the peak-to-valley formula for α provides 12.4 mrad as the optimal value. Assuming that the intensity cross-section measurement in Fig. 2b is approximately proportional to the thickness of the membrane, we find that it fits well (dashed red line) to a fourth degree polynomial ($R^2 = 0.986$).

Fig. 2c considers only diffraction, chromatic, and spherical aberrations, as a function of the semi-convergence angle α . Each diameter is calculated using the 50% current-enclosed criterion and combined using a root power sum method [21], as follows. Diffraction broadens the probe for lower values of α according to $d_{d50} = 0.54\lambda/\alpha$. For larger α , spherical aberration dominates with a cubic dependence as $d_{s50} = 0.18C_s\alpha^3$, while the contribution from chromatic aberration $d_{c50} = 0.34C_c(\Delta E/E)\alpha$ is linear. The combined probe diameter then takes the form [21] $((d_{d50}^4 + d_{s50}^4)^{1.3/4} + d_{c50}^{1.3})^{2/1.3} + d_{c50}^2)^{1/2}$. Broadening due to spatial incoherence is included in the term d_{i50} , but is experimentally negligible since we use a highly demagnified source. Fig. 2c shows an expected optimum (marked “o”) for an uncorrected probe at 6.4 mrad with a diameter of 180 pm. We used $C_c = C_s = 2.7$ mm, and $\Delta E = 0.8$ eV, as measured in a separate electron energy-loss spectroscopy (EELS) experiment. The corresponding value for a corrected probe is 12.4 mrad with a diameter of 91 pm (marked “x”). Given that the corrector’s radius r_{max} is fixed, the compensated curve (dashed purple line), is calculated using $C_{s,eff}(\alpha) = C_s + C_{s,\Lambda=2}(\alpha)$, where $C_{s,\Lambda=2}(\alpha) = 32\lambda/\alpha^4$ is the spherical aberration introduced by the corrector. $C_{s,eff}(\alpha)$ is now the combined spherical aberration coefficient of the microscope and the thin film corrector. It compensates spherical aberration ($C_{s,eff}(\alpha) = 0$) for one, optimal value of α . It is important to note that these semi-quantitative estimates are design guidelines, and that rigorous probe modeling requires a complete wave-optical numerical simulation. Possible deviations from the expected values of C_s and C_c , from the intended overall thickness in fabrication, or from usage of the corrector at a different accelerating voltage, would only result in a different optimal value for α . Experimentally, we found optimal values of 7.46 mrad and 12.1 mrad for the uncorrected and corrected microscope, respectively.

3. Corrector fabrication

Our material of choice for the refractive thin film corrector is presently a commercially available 200-nm-thick silicon nitride (SiN) film on a 200- μm -thick Si substrate frame. We use SiN because it provides a good trade-off between scattering, phase shifting, and mechanical robustness. The window size must be at least 2–3 times as large as the corrector diameter, so that appreciable electrostatic fields do not develop on the sharp corners of the selectively-etched substrate walls, as this would result in the introduction of high-order aberrations; in particular, we observed four-fold astigmatism, which we attribute to the square geometry of the etched window.

For a 50- μm -diameter corrector, a commercial 100–250 μm window was found to suffice. In our experiment, we desired many such windows on one 3 mm chip, which we could not obtain commercially. We therefore used a photolithography process to create our own chips with 9 large window membranes. We began with a 250 μm Si wafer coated with 200 nm of low-pressure chemical vapor-deposited SiN (UniversityWafer, Inc.). We photolithographically defined apertures on one (“flat”) side, coated with 2 nm Cr and 150 nm Au, and performed lift-off, then defined the windows on the other (“window”) side. The wafer was initially etched

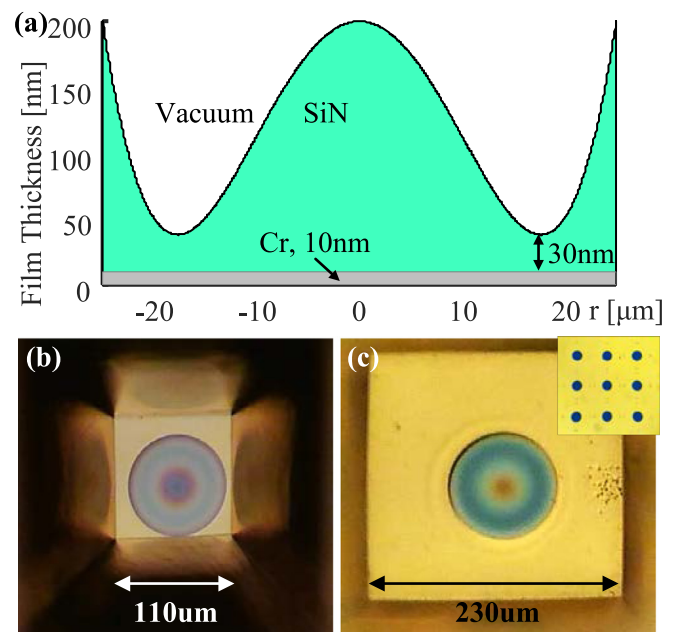


Fig. 3. (Colour online) (a) Calculated thin film corrector profile, with 10 nm Cr for charge alleviation (gray, bottom) and milled SiN (green, top). We estimate that approximately 30 nm of unmilled SiN remains to mechanically support the structure. (b,c) Example optical microscope images of the window side of one window of (b) a commercial membrane with a 110 μm edge, and (c) our in-house-fabricated membrane with a 230 μm edge. Inset: flat side showing 9 open apertures of bare SiN (blue) in the Au layer (yellow). Both are formed from 200 nm of SiN, coated with Cr and Au from the window side, and show a milled 100 μm corrector. In (c), there is faint evidence of the 120 μm -diameter aperture on the flat side’s Au layer. Varying colors result from different illumination conditions. The contrast and brightness have been changed for visibility. In (b), we did not have a Au layer on the flat side.

through ~ 230 μm of its thickness using a deep-reactive ion-etching machine. The process was completed by performing a couple of hours of KOH etching.

The etched window side of the membrane was then similarly coated with a 2 nm Cr and a 150 nm Au. The purpose of this layer is to reduce excess charge build-up by enhancing conductivity, but, more importantly, to strongly scatter incident electrons, and in principle to thus act as a strong (opaque) amplitude mask [18], or diaphragm, since beyond the corrector’s radius r_{max} the beam retains its high spherical aberration. The corrector structure was milled directly through this layer, which could be easily and completely removed owing to the much higher sputtering rate of Au, compared to SiN. Milling was performed using a Raith IonLine Gallium FIB operated at 35 kV with an 800 pA beam current.

The beam dwell time during FIB milling translates to depth in an approximately linear manner (although an accurate calibration could be employed), resulting in a surface profile that is defined according to Eq. (3). Assuming, per our design, that $\Lambda = 2$, $r_{max} = 25$ μm , and $t_{2\pi} = 85$ nm for SiN at 300 keV, the calculated profile is shown in Fig. 3a. This value for $t_{2\pi}$ was inferred from measurements using off-axis electron holography of SiN films taken from the same batch as those used for fabrication of the corrector; however, the exact value is not important and any deviation would only result in a slightly different optimal convergence angle α .

As a final step, we coated the membrane with 10 nm of Cr on the flat side for good measure, since bare SiN is insulating. The Cr layer is shown in Fig. 3a, along with an estimated 30 nm of unmilled SiN left as a mechanical support.

We produced both 50- μm -diameter and 100- μm -diameter correctors in this way. The differences between a commercial mem-

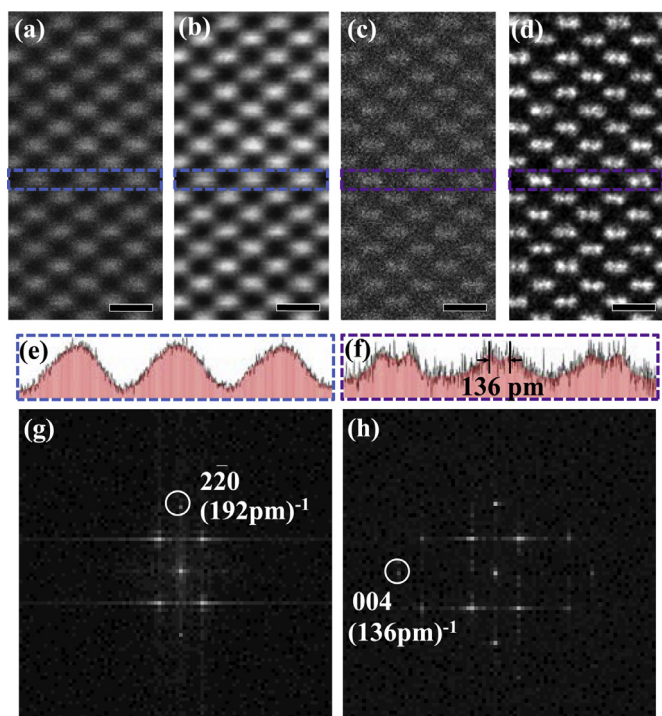


Fig. 4. HAADF STEM images of Si (110) were recorded without (a,b,e,g) and with (c,d,f,h) the thin film corrector. Images were denoised slightly (b,d) from the raw data (a,c). Intensity profiles of the marked regions in (a,b) and (c,d) are plotted in (e) and (f), respectively, showing the raw data as black lines and denoised data as pink histograms. (g) and (h) show the Fourier spectrum of the unprocessed images (a) and (c). Only after correction does the 136 pm-separated Si dumbbells become visible, both in the HAADF STEM image and in its Fourier spectrum. The scale bars in (a–d) are 500 pm.

brane ($\sim 110 \mu\text{m}$ edge) and our membrane ($\sim 230 \mu\text{m}$) are shown in the form of optical microscope images in Fig. 3b and Fig. 3c, respectively. In Fig. 3c, one can notice the faint circumference of a 120 μm aperture fabricated on the flat side of this specific membrane in the photolithography step.

4. Correction assessment

We fabricated our thin film corrector using FIB milling and installed it in the Condenser 2 aperture position in a 300 kV ($\lambda = 1.97 \text{ pm}$) FEI Titan microscope [22], with a known spherical aberration coefficient, $C_s = 2.7 \text{ mm}$. This microscope is equipped with a CEOS *post-specimen* spherical aberration corrector. As such, it cannot correct the *pre-specimen* illumination optics (that is, it is not a probe-corrected microscope) and therefore has no advantageous effect on STEM measurements. In order to test the performance of our corrector, we recorded high-angle annular dark-field (HAADF) STEM images of crystalline Si in a $\langle 110 \rangle$ orientation both without (Fig. 4a,b,e,g) and with (Fig. 4c,d,f,h) the corrector.

Fig. 4b and d are noise-filtered images of Fig. 4a and c using a non-linear denoising algorithm with the same processing parameters [23]. Fig. 4e and f plot the intensity profile of the marked region in Fig. 4a–d, respectively, showing the raw data as black lines and the denoised data as pink histograms. Fig. 4g and h show the Fourier transform power spectra of the unprocessed images, Fig. 4a and c. An improvement in spatial resolution is clearly visible in both real and Fourier space, allowing 136-pm-separated dumbbells to be resolved. Appendix A contains more details on the analysis of the noise filtering (Fig. S1), as well as results recorded from an additional sample that demonstrates 128 pm spatial resolution (Fig. S2).

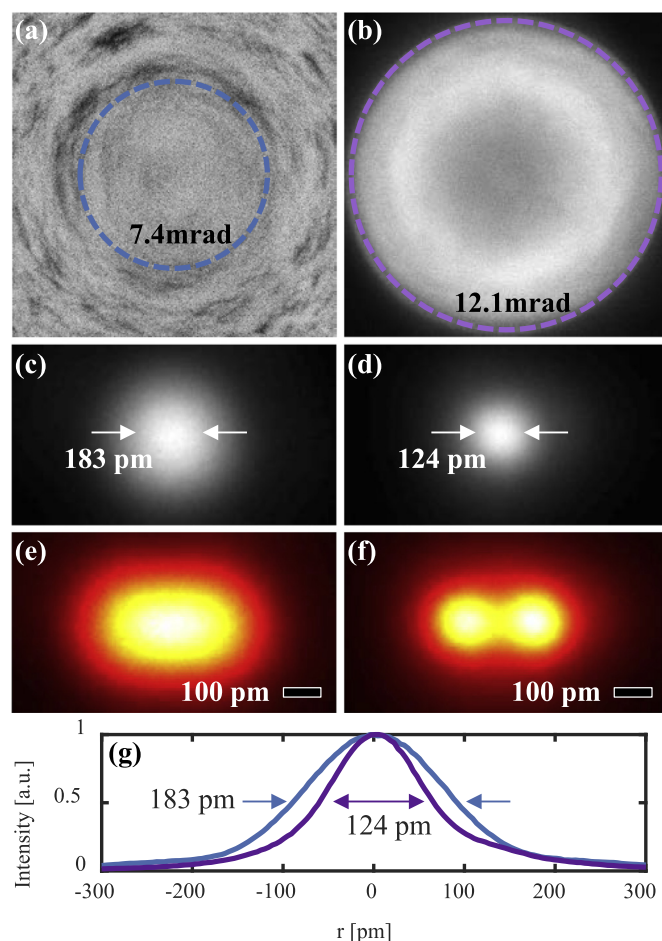


Fig. 5. (Colour online) Spherical correction assessment. (a, b) Experimental Ronchigrams recorded from amorphous C to measure the aberration-free angle: (a) uncorrected, limited to 7.4 mrad and (b) corrected to 12.1 mrad. (c, d) Corresponding full width at half maximum probe measurements: (c) uncorrected (183 pm), (d) corrected (124 pm). (e, f) Simulations of 136-pm-separated points using the (e) uncorrected, and (f) corrected probe measurements. Only the corrected probe is able to resolve the test object. (g) Cross-sections of the uncorrected and corrected probes in blue and purple, respectively, averaged over 60 pm. The maximum intensities of the profiles are normalized to unity, in order to compare their widths.

Spherical aberration in a STEM probe can also be inferred from an electron Ronchigram [24], which involves recording the diffraction pattern of a stationary probe, focused on the sample (here, an amorphous C film). Both the convergence semi-angle α and the aberrations are revealed in such an image. In particular, spherical aberration [25] is recognizable from radii and azimuths of infinite magnification, as shown in Fig. 5a, which was recorded without using the corrector. A focused spherical-aberration-free probe produces a Ronchigram that resembles a flat, nearly-uniformly-illuminated disc, which is associated with a nearly constant phase distribution - similar to the image shown in Fig. 5b, which was recorded using our corrector.

According to Scherzer [3], the required convergence semi-angle α for achieving optimal resolution is $1.41(\lambda/C_s)^{1/4} \approx 7.34 \text{ mrad}$, in agreement with the value of 7.46 mrad used in our experiment. The corrector is presently designed to correct spherical aberration at and up to $\alpha \approx 12 \text{ mrad}$, as shown in Fig. 5b. Appendix B shows a through-focus series of Ronchigrams at different convergence angles recorded from both amorphous and crystalline material.

Measurements of the uncorrected and corrected probes and their line profiles (Fig. 5) demonstrate a decrease of more than 30% in diameter. For this measurement, the microscope should ideally

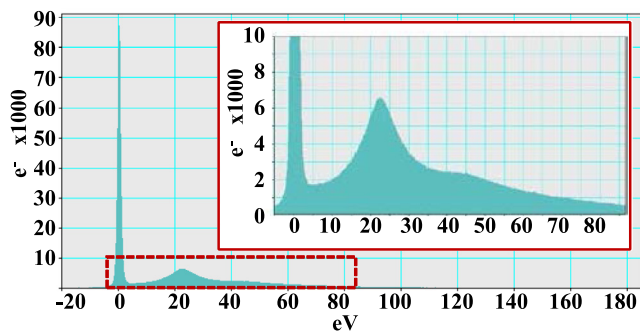


Fig. 6. EELS measurement obtained from a corrected electron probe in vacuum. The inset shows an enlargement of the dashed region. A broad distribution of energy losses is visible, with a prominent plasmon peak at $\Delta E = 23$ eV. The second peak at $\Delta E = 45$ eV most probably results from plural scattering.

be spherical-aberration-free from the sample plane to the detector. The post-specimen CEOS corrector was used to correct monochromatic image aberrations up to approximately 15 mrad. Therefore, our direct probe measurements are expected to be only slightly smeared by the chromatic aberration of the objective lens. We then used the measured probes to simulate two points separated by 136 pm, representing Si dumbbells, in order to confirm the formation of irresolvable and resolvable images in Fig. 5e and f, respectively.

5. Effect of inelastic scattering on the electron probe and STEM imaging

A key challenge in the present concept is scattering by the material-based thin film corrector, which is manifested in the Ronchigram in Fig. 5b as a faint amplitude modulation, resulting from the annular thickness variation of the corrector (see also Fig. 2a). As elaborated below, it does not contribute to enhanced resolution, and is the only mechanism that affects otherwise 100%-efficient intensity transfer to the corrected probe. We used EELS to determine t/λ [26] in silicon nitride at 300 kV to be approximately 1.15, with an energy distribution comprising typical losses of 10–50 eV. The angular distribution of inelastic scattering leaving the corrector has an axially sharp peak and a broad tail that reaches far beyond 50 mrad, resulting in a noisy background and a loss of contrast in STEM images. Whereas the intensity of the sharp peak is only appreciable for angles θ much smaller than the characteristic angle for elastic scattering [27], the spatial distribution in the sample plane in proximity to the probe is negligible, since the typical transverse distance of scattered electrons θf is several orders of magnitude larger than the diameter of the probe, where f is the equivalent focal length of the probe-forming optics. Since most of the contrast degradation is due to the large-area inelastic tail, it could be reduced by mounting a small aperture on the sample itself, or by designing the probe-forming optics with another aperture near a crossover above the sample. Inelastic scattering could also be mitigated and the contrast improved using a fractured, thinner design [17] or a different material [20].

In order to fully understand this effect, additional measurements and simulations were performed. Fig. 6 shows a recorded electron energy-loss spectrum of a corrected probe in vacuum. The probe convergence semi-angle α was 12.1 mrad and the spectrometer acceptance semi-angle was 17.3 mrad. The energy-loss distribution shows a plasmon peak at $\Delta E = 23$ eV. An additional small peak visible at $\Delta E = 45$ eV most probably results from plural scattering. Integration of the intensities in the zero-loss peak and the inelastic electrons provides a value for the ratio of elastic to inelastic scattering of approximately 0.66.

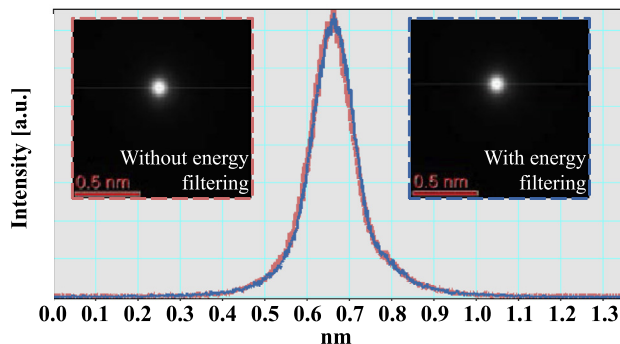


Fig. 7. (Colour online) Profiles of a corrected probe with (blue) and without (red) the use of zero-loss energy filtering. The energy filter slit width used was 10 eV.

The broad energy range of the electron probe clearly limits its application to EELS measurements, as the EELS signal that leaves the silicon nitride thin film, which includes the plasmon peak and the Si and N core loss peaks, will be superimposed on any spectrum obtained from the specimen. Furthermore, energy-loss electrons could produce a “shadow spectrum” with a tiny energy shift compared to those generated by elastic electrons, leading to a deterioration in energy resolution. These two difficulties can in principle be overcome by recording a reference spectrum in vacuum and post-processing the spectrum collected from the specimen using a deconvolution algorithm. However, this task is challenging and is dependent on the specimen used.

In contrast, there is no problem to combine energy dispersive X-ray spectroscopy (EDS) with our thin film corrector, since the X-ray signals from the corrector are far from the EDS detection region and the energy resolution of EDS is usually more than 100 eV.

The influence of inelastic scattering on a corrected probe profile was measured using a Gatan Imaging Filter (GIF). Similarly to Fig. 5d, additional measurements were recorded using an energy filtering slit of width 10 eV centered on the zero-loss peak, such that the image was formed from only elastically scattered electrons.

Fig. 7 compares the probe with and without filtering. There is no perceivable difference in the peak profile of the corrected probe. The inelastically scattered electrons, therefore, affect only the tail of the probe, which is smeared over a very large area with relatively low intensity, and contributes to background noise during scanning. This is why the use of an aperture in the specimen plane may provide an approach for decreasing inelastic scattering noise in such images significantly.

We performed a simulation to estimate the effect of inelastic scattering on HAADF STEM images using μ STEM software [28]. The microscope parameters in the simulation were: $E_0 = 300$ keV; C_s corrected; $C_c = 2.7$ mm (as for the microscope that we used); $\alpha = 12.4$ mrad; inner collection semi-angle = 80 mrad. The simulated specimen was Si in a (110) orientation. The size of each simulated image was 256×182 pixels, or 1055×750 pm. We assumed that an image formed by electrons that have been inelastically scattered in the silicon nitride thin film is equivalent to an image that is defocused as a result of chromatic aberration C_c and energy loss ΔE . The defocus is calculated to be $\Delta E/E_0 \cdot C_c$. In order to simplify the simulation, we used a single plasmon peak energy of 23 eV for ΔE , rather than the true broad energy distribution of the plasmon peak. The final image obtained using the thin film corrector was an average of the focused (elastic) and defocused (inelastic) images, which were combined with a weighting factor of 0.66:1, according to the ratio mentioned above (see Fig. 6).

A simulated conventional aberration-corrected HAADF STEM image and one that includes inelastic scattering in the thin film

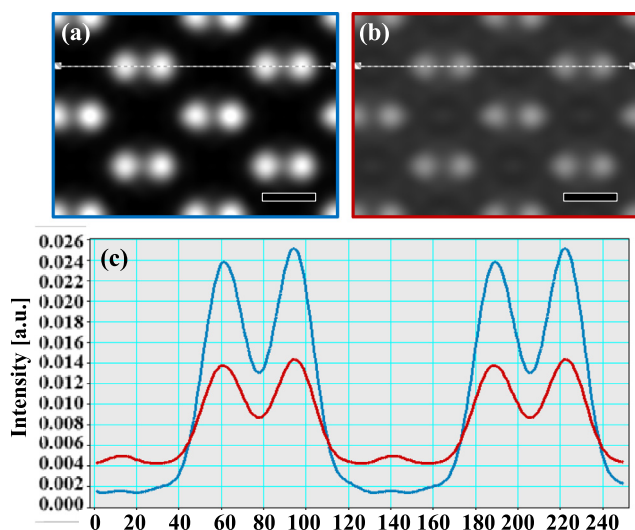


Fig. 8. (Colour online) (a) Simulated conventional aberration-corrected HAADF STEM image of dumbbells in Si in a (110) orientation. (b) Simulated HAADF STEM image of the same specimen including the effect of inelastic scattering in a thin film corrector. Both images are displayed with the same intensity range (0–0.025), so as to compare their contrast. Both scale bars are 200 pm. (c) Line profile across the Si dumbbells from images (a) (blue) and (b) (red). The units of the x axis are pixels, where 1 pixel corresponds to 4.12 pm.

corrector are shown in Fig. 8. Based on the line profiles across the Si dumbbells, one can conclude that, when using a thin film corrector, the maximum intensity is decreased by 43% and the contrast $(N_{\max} - N_{\min}) / (N_{\max} + N_{\min})$ drops from 89% to 53%. If the maximum intensity is normalized to the same value, then the peak to valley height of the dumbbell also drops by 19%. These results *qualitatively* explain the contrast reduction of our experimental measurements when compared with those obtained using a commercial corrector (see Appendix C).

6. Discussion

A frequent concern with the use of thin film phase plates, in addition to scattering, is the issue of contamination. Phase plates used for contrast enhancement and placed in the high intensity back focal plane of the objective lens differ from our thin film, which is placed in the Condenser 2 plane and is expected to experience a current density approximately 10 orders of magnitude smaller [17], thereby greatly diminishing charging and contamination. Repeated experiments spanning over 100 h of irradiation using a 52 pA beam current (see Appendix A) showed no noticeable deterioration in performance. Contamination strongly affects the behavior of charged foils [9] and phase plates [29–31], since any contamination build-up, even on the sub-nm scale, can interfere with the distribution of surface charge that is responsible for the desired electric field distribution. On our corrector, we expect contamination to be distributed homogeneously along the circumference of illumination of the corrector (which is always much larger than the corrector diameter, estimated to be 300 μm in Condenser 2), and that its effect will be negligible when compared to the thin film's refractive properties. Moreover, in support of our claim of robustness, we did not perform any kind of cleaning (plasma or other) before installing the corrector in the microscope.

Thin-film-based correctors of the present design are also advantageous in that their fabrication is independent of the intended accelerating voltage and their thickness profile has no strict tolerance. A change in these parameters will only result in a shift of the corrector's operating semi-convergence angle α (controlled by the excitation of the microscope's probe-forming lenses) and the

strength of correction. The corrector will then negate the spherical aberration for a new value of α .

A further advantage of the present design is that it corrects the electron probe on-axis, requiring practically no change in the standard measurement procedure. A different approach for shaping electron beams involves an off-axis scheme that is based on computer-generated holography [32,33] and on the use of binary masks, which can also be used to introduce or negate aberrations. However, manipulation is then performed on the first diffraction order, which limits the theoretically accessible intensity to 10% and 40% for binary amplitude and phase structures, respectively. All other diffraction orders must be filtered out from reaching the sample, meaning that the installation and operation of such a corrector requires additional electron-optical elements and protocols for STEM imaging, which may not be readily reproducible by the average user [34] and have not yet shown practical improvement [35,36]. Furthermore, the efficiency figures would be diminished by approximately 80% due to unavoidable inelastic scattering, reducing the usable intensity and current in the corrected probe. The fabrication of non-binary structures, such as blazed gratings, is still difficult to implement [37,38].

7. Conclusion

We have shown spherical aberration correction and resolution enhancement using a thin film of variable thickness in STEM. In-house fabrication and implementation in an existing uncorrected microscope is demonstrated, without changing standard operating procedures. The use of other weakly scattering materials [20], as well as thinner or fractured designs and spatial filtering, can further reduce the effect of inelastically scattered electrons and improve STEM image contrast. The correction of additional aberrations is possible by appropriately designing the thickness profile. A similar approach can in principle also be applied to TEM imaging.

Acknowledgments

This work was supported by the Israel Science Foundation (grant no. 1310/13) and by the German-Israeli Project cooperation (DIP). The research leading to these results has received funding from the European Research Council under the European Union's Seventh Framework Programme (FP7/2007–2013)/ERC grant agreement number 320832. The authors are grateful to Chris B. Boothroyd, Juri Barthel, Emrah Yucelen and Christian Dwyer for valuable discussions on this work, and to Les J. Allen for assistance with inelastic scattering simulations.

Appendix A. HAADF STEM imaging: noise filtering and additional 128 pm measurements

Fig. S1 shows HAADF STEM images of Si (110) that were recorded at 300 keV using a Fischione Model 3000 HAADF detector both with (left column) and without (right column) the thin film corrector. The inner and outer detection angles of the HAADF detector were ~ 50 and ~ 200 mrad, respectively. The dwell time was 1 μs per pixel. The probe current was ~ 52 pA without corrector and ~ 7 pA with corrector, as measured with a Faraday Cup. All of the images are single scans, rather than multi-frame averages. A nonlinear filtering algorithm [23] was applied to the raw images recorded both with (Fig. S1a) and without (Fig. S1h) the thin film corrector. The same filtering parameters were used in each case. Filtered images, which correspond to Fig. 4d and b in the main text, are shown in Fig. S1c and Fig. S1j, respectively. We justify the use of slight noise-filtering in two ways. First, there are no features in the noise images (Fig. S1e and Fig. S1l), which reveal differences

between the raw data and the filtered data. The contrast of the difference images is deliberately enhanced to help judge if there is any periodic feature. The autocorrelations of the difference images (Fig. S1f and Fig. S1m) are characterized by a delta-function profile of their central cross sections (Fig. S1g and Fig. S1n), which normally results from ideally uncorrelated noise rather than periodic features. Second, the characteristic spatial frequency, $(136 \text{ pm})^{-1}$, which corresponds to the dumbbell separation, can be clearly seen in the Fourier transform power spectra of both the unfiltered (Fig. S1b) and the filtered (Fig. S1d) spherical-aberration-corrected images. Without correction, the highest spatial frequencies that are achieved in both the unfiltered (Fig. S1g) and the filtered (Fig. S1i) images are also the same, but are reduced to $(192 \text{ pm})^{-1}$. The resolvable dips between the dumbbell peaks in the cross-section profile shown in Fig. 4f in the main text, together with the aforementioned extension in spatial frequency, confirm that the separation of 136 pm dumbbells has been realized using the thin film corrector. We note that sub-Ångström resolution appears to be implied by the presence of a $(96 \text{ pm})^{-1}$ (4–40) spot in Fig. S1d, which, however, is not present in Fig. S1b. A cause could be a nonlinear effect related to the experimental black level, which is discussed comprehensively in [39].

A Cu nanocrystalline sample in a $\langle 112 \rangle$ orientation was also measured in HAADF STEM imaging mode using the thin film corrector. Based on the Fourier power spectra shown in Fig. S2b and Fig. S2d, one can notice the presence of a (2–20) spot. In the filtered image shown in Fig. S2c, the 128-pm-separated (2–20) lattice can be clearly resolved in the horizontal direction. Although the ability to resolve the periodicity in the raw image is arguable, the filtered image in Fig. S2c, the spectrum in Fig. S2d and the noise difference image in Fig. S2e as well as its autocorrelation, Fig. S2f, with a delta-function central cross-section profile, Fig. S2g, all demonstrate sub-130-pm resolution.

Appendix B. Ronchigram evaluation using through-focus series of amorphous and crystalline materials

Fig. S3 shows through-focus series of Ronchigrams collected from an amorphous C film for different values of α using the thin film corrector. The Ronchigram is cut off by the diaphragm and usually contains spherical aberration rings and a shadow image inside the rings, which should look smooth at infinite magnification near focus (corresponding to a so-called “sweet spot”, or aberration-free region). In our case, the center is always darker as a result of the thickness variation of the thin film corrector. As the thin film corrector introduces a spatial phase modulation regardless of the instrument’s chosen α , it will over-correct at lower α and under-correct at higher α , with both situations leading to a larger probe diameter or a smaller aberration-free angle (see also Fig. 2c). At 12 mrad (Fig. S3c), the spherical aberration rings can hardly be seen, since this is the optimal value of α (by design), and the aperture clips the wavefront just inside the rings. At a lower α of 8 mrad (Fig. S3a), the aberration-free angle is only 3.3 mrad, while at a higher α (Fig. S3c-d) it is also less than 12 mrad. It should be noted that, for a standard circular aperture in this microscope, the aberration-free angle is approximately 7.4 mrad (Fig. 5a) and does not change dramatically with α . Analysis of these measurements (Fig. 2c) confirms that our thin film corrector operates in accordance with its design.

It may be argued that the observed resolution enhancement is not due to a phase correction of the beam’s wavefront, but due to an amplitude modulation resulting from the varying thickness of the corrector. An appropriate amplitude modulation could favorably influence and assist to resolve a certain band of spatial frequencies, at the cost of strongly diminishing or eliminating the contrast of others. Since the magnification M in a Ronchigram is

dependent on the defocus Δz relative to the corrector plane and the spherical aberration as $1/M = \Delta z + 3C_s\theta^2$, amplitude modulation would destroy the fringe contrast. Moreover, if C_s is properly corrected, the magnification should be uniform across the Ronchigram, for any defocus value. As such, it is proposed to examine a crystalline material.

Fig. S4–Fig. S7 show defocus series of a SrTiO₃ $\langle 100 \rangle$ crystal recorded without (Fig. S4) and with (Fig. S5–Fig. S7) our corrector. We chose this crystal since it has a square lattice, such that distortions are easily recognized. Only when our corrector is utilized in the optimal α (12 mrad) is the magnification constant across the angular range (Fig. S6). Furthermore, for all defoci the contrast of the lattice pattern, albeit impaired (as a result of inelastic scattering), is only very slightly modulated except at the very edge of the corrector. This result proves that, when our corrector is used, there is no significant spherical aberration. Once the wavefront’s phase is corrected, amplitude variation cannot help to achieve high resolution. On the contrary, for a perfect phase front amplitude modulation can only decrease the resolution. Therefore, our demonstration of resolution enhancement is not a result of amplitude modulation.

Appendix C. Comparison with a commercial aberration corrector

Here, we compare images of a Si sample in a $\langle 110 \rangle$ orientation recorded using our thin film corrector and a commercial multi-pole corrector. An HAADF STEM image (Fig. S8a) was recorded using an FEI Titan G2 80–200 ChemiSTEM microscope equipped with a high brightness field emission gun and a commercial electromagnetic probe spherical aberration corrector (DCOR, CEOS GmbH) at 200 kV. The convergence semi-angle was 24.7 mrad and the inner collection semi-angle was 88 mrad. The dwell time was 2 $\mu\text{s}/\text{pixel}$. It should be noted that Fig. S8a is a raw image without any post-processing. A Fourier transform and a line profile showing the Si dumbbells are also shown in Fig. S8b and Fig. S8c. A comparison with the results in Fig. 4 and Fig. S1 taken using the thin film corrector indicates that the commercial electromagnetic spherical aberration corrector provides better contrast than the thin film corrector, although the latter is still able to resolve similar features.

Supplementary materials

Supplementary material associated with this article can be found, in the online version, at doi:10.1016/j.ultramic.2018.03.016.

References

- [1] M. Knoll, E. Ruska, Das Elektronenmikroskop, Zeitschrift Für Phys. 78 (1932) 318–339, doi:10.1007/BF01342199.
- [2] O. Scherzer, Über einige Fehler von Elektronenlinsen, Zeitschrift Für Phys. 101 (1936) 593–603, doi:10.1007/BF01349606.
- [3] O. Scherzer, The theoretical resolution limit of the electron microscope, J. Appl. Phys. 20 (1949) 20–29, doi:10.1063/1.1698233.
- [4] M. Haider, H. Rose, S. Uhlemann, E. Schwan, B. Kabius, K. Urban, A spherical-aberration-corrected 200kV transmission electron microscope, Ultramicroscopy 75 (1998) 53–60, doi:10.1016/S0304-3991(98)00048-5.
- [5] O.L. Krivanek, N. Dellby, A.R. Lupini, Towards sub-Å electron beams, Ultramicroscopy 78 (1999) 1–11, doi:10.1016/S0304-3991(99)00013-3.
- [6] S.J. Pennycook, The impact of STEM aberration correction on materials science, Ultramicroscopy 180 (2017) 22–33, doi:10.1016/j.ultramic.2017.03.020.
- [7] P.W. Hawkes, Aberration correction past and present, Philos. Trans. R. Soc. A Math. Phys. Eng. Sci. 367 (2009) 3637–3664, doi:10.1098/rsta.2009.0004.
- [8] A.A. van Gorkum, L.C.M. Beirens, Experiments on eliminating spherical aberration in electron guns using aspherical mesh lenses, J. Vac. Sci. Technol. A Vacuum, Surfaces, Film. 4 (1986) 2297–2306, doi:10.1116/1.574067.
- [9] T. Hanai, H. Yoshida, M. Hibino, Characteristics and effectiveness of a foil lens for correction of spherical aberration in scanning transmission electron microscopy, J. Electron Microsc. (Tokyo) 47 (1998) 185–192. <http://dx.doi.org/10.1093/oxfordjournals.jmicro.a023579>.
- [10] H. Boersch, Über die Kontraste von Atomen im Elektronenmikroskop, Zeitschrift Fur Naturforsch. - Sect. A J. Phys. Sci. 2 (1947) 615–633, doi:10.1515/zna-1947-11-1204.

- [11] M. Beleggia, L.C. Gontard, R.E. Dunin-Borkowski, Local charge measurement using off-axis electron holography, *J. Phys. D. Appl. Phys.* 49 (2016) 294003, doi:[10.1088/0022-3727/49/29/294003](https://doi.org/10.1088/0022-3727/49/29/294003).
- [12] K. Nagayama, Another 60 years in electron microscopy: development of phase-plate electron microscopy and biological applications, *Microscopy* 60 (2011) S43–S62, doi:[10.1093/jmicro/dfr037](https://doi.org/10.1093/jmicro/dfr037).
- [13] D. Willasch, High-resolution electron-microscopy with profiled phase plates, *Optik (Stuttg)* 44 (1975) 17.
- [14] K. Müller, Phase Plates for Electron-Microscopes, *Optik (Stuttg)* 45 (1976) 73.
- [15] A.L. Bleloch, Y. Ito, L.M. Brown, *Nature* 394 (1998) 49–52, doi:[10.1038/27863](https://doi.org/10.1038/27863).
- [16] R. Shiloh, Y. Lereah, Y. Lilach, A. Arie, Sculpturing the electron wave function using nanoscale phase masks, *Ultramicroscopy* 144 (2014) 26–31, doi:[10.1016/j.ultramic.2014.04.007](https://doi.org/10.1016/j.ultramic.2014.04.007).
- [17] R. Shiloh, R. Remez, A. Arie, Prospects for electron beam aberration correction using sculpted phase masks, *Ultramicroscopy* 163 (2016) 69–74, doi:[10.1016/j.ultramic.2016.02.002](https://doi.org/10.1016/j.ultramic.2016.02.002).
- [18] R. Shiloh, A. Arie, 3D shaping of electron beams using amplitude masks, *Ultramicroscopy* 177 (2017) 30–35, doi:[10.1016/j.ultramic.2017.02.001](https://doi.org/10.1016/j.ultramic.2017.02.001).
- [19] W.J. Smith, *Modern Optical Engineering, third ed.*, McGraw-Hill, 2000.
- [20] M. Dries, S. Hettler, T. Schulze, W. Send, E. Müller, R. Schneider, et al., Thin-film phase plates for transmission electron microscopy fabricated from metallic glasses, *Microsc. Microanal.* 22 (2016) 955–963, doi:[10.1017/S143192761601165X](https://doi.org/10.1017/S143192761601165X).
- [21] J.E. Barth, P. Kruij, Addition of different contributions to the charged particle probe size, *Optik (Stuttg)* 101 (1996) 101–109.
- [22] C. Boothroyd, A. Kovács, K. Tillmann, FEI Titan G2 60–300 HOLO, *J. Large-Scale Res. Facil. JLSRF* 2 (2016) A44, doi:[10.17815/jlsrf-2-70](https://doi.org/10.17815/jlsrf-2-70).
- [23] H. Du, A nonlinear filtering algorithm for denoising HR(S)TEM micrographs, *Ultramicroscopy* 151 (2015) 62–67, <http://dx.doi.org/10.1016/j.ultramic.2014.11.012>.
- [24] V. Ronchi, Forty years of history of a grating interferometer, *Appl. Opt.* 3 (1964) 437–451, doi:[10.1364/AO.3.000437](https://doi.org/10.1364/AO.3.000437).
- [25] J.A. Lin, J.M. Cowley, Calibration of the operating parameters for an HB5 stem instrument, *Ultramicroscopy* 19 (1986) 31–42, doi:[10.1016/0304-3991\(86\)90005-7](https://doi.org/10.1016/0304-3991(86)90005-7).
- [26] T. Malis, S.C. Cheng, R.F. Egerton, EELS log-ratio technique for specimen-thickness measurement in the TEM, *J. Electron Microsc. Tech* 8 (1988) 193–200, doi:[10.1002/jemt.1060080206](https://doi.org/10.1002/jemt.1060080206).
- [27] L. Reimer, H. Kohl, *Transmission Electron Microscopy*, Springer New York, New York, NY, 2008, doi:[10.1007/978-0-387-40093-8](https://doi.org/10.1007/978-0-387-40093-8).
- [28] L.J. Allen, A.J. D'Alfonso, S.D. Findlay, Modelling the inelastic scattering of fast electrons, *Ultramicroscopy* 151 (2015) 11–22 <http://dx.doi.org/>, doi:[10.1016/j.ultramic.2014.10.011](https://doi.org/10.1016/j.ultramic.2014.10.011).
- [29] K. Danov, R. Danev, K. Nagayama, Reconstruction of the electric charge density in thin films from the contrast transfer function measurements, *Ultramicroscopy* 90 (2002) 85–95 [https://doi.org/10.1016/S0304-3991\(01\)00143-7](https://doi.org/10.1016/S0304-3991(01)00143-7).
- [30] R. Danev, B. Buijsse, M. Khoshouei, J.M. Plitzko, W. Baumeister, Volta potential phase plate for in-focus phase contrast transmission electron microscopy, *Proc. Natl. Acad. Sci. U. S. A.* 111 (2014) 15635–15640, doi:[10.1073/pnas.1418377111](https://doi.org/10.1073/pnas.1418377111).
- [31] S. Hettler, M. Dries, P. Hermann, M. Obermair, D. Gerthsen, M. Malac, Carbon contamination in scanning transmission electron microscopy and its impact on phase-plate applications, *Micron* 96 (2017) 38–47 <https://doi.org/10.1016/j.micron.2017.02.002>.
- [32] B. Brown, A. Lohmann, Complex spatial filtering with binary masks, *Appl. Opt.* 5 (1966) 967–969.
- [33] W. Lee, in: *Binary computer-generated holograms*, 18, 1979, p. 3661.
- [34] D. Pohl, S. Schneider, P. Zeiger, J. Ruzs, P. Tiemeijer, S. Lazar, et al., Atom size electron vortex beams with selectable orbital angular momentum, *Sci. Rep.* 7 (2017) 934, doi:[10.1038/s41598-017-01077-9](https://doi.org/10.1038/s41598-017-01077-9).
- [35] M. Linck, P.A. Ercius, J.S. Pierce, B.J. McMorrán, Aberration corrected STEM by means of diffraction gratings, *Ultramicroscopy* 182 (2017) 36–43, doi:[10.1016/j.ultramic.2017.06.008](https://doi.org/10.1016/j.ultramic.2017.06.008).
- [36] V. Grillo, A.H. Tavabi, E. Yucelen, P.-H. Lu, F. Venturi, H. Larocque, et al., Towards a holographic approach to spherical aberration correction in scanning transmission electron microscopy, *Opt. Express* 25 (2017) 21851, doi:[10.1364/OE.25.021851](https://doi.org/10.1364/OE.25.021851).
- [37] T.R. Harvey, J.S. Pierce, A.K. Agrawal, P. Ercius, M. Linck, B.J. McMorrán, Efficient diffractive phase optics for electrons, *New J. Phys.* 16 (2014) 93039, doi:[10.1088/1367-2630/16/9/093039](https://doi.org/10.1088/1367-2630/16/9/093039).
- [38] V. Grillo, G. Carlo Gazzadi, E. Karimi, E. Mafakheri, R.W. Boyd, S. Frabboni, Highly efficient electron vortex beams generated by nanofabricated phase holograms, *Appl. Phys. Lett* 104 (2014) 43109, doi:[10.1063/1.4863564](https://doi.org/10.1063/1.4863564).
- [39] Z. Yu, P.E. Batson, J. Silcox, Artifacts in aberration-corrected ADF-STEM imaging, *Ultramicroscopy* 96 (2003) 275–284, doi:[10.1016/S0304-3991\(03\)00093-7](https://doi.org/10.1016/S0304-3991(03)00093-7).